

EISCAT_3D Project
WP5 Final Report
Aperture Synthesis Imaging Radar, ASIR
University of Tromsø, Department of Physics
Draft — May 2009

1. Summary

The built-in interferometric capabilities of the EISCAT_3D system—complemented with multiple beams and rapid beam scanning—is what will make the new radar truly three dimensional and justify its name. Work Package 5 provides the basic foundations upon which the imaging capabilities will be implemented. The conditions and parameters for the new radar to have a 3-Dimensional capability have been established. The core antenna will be composed of about 20 or more modules (sets of 343 antenna elements) accompanied by a few outlying modules, the latter to comply with the resolution requirements. This is an optimum and flexible antenna layout from which favourable configurations can be quickly implemented to obtain the resolution and bandwidth of the required image; several simulated configurations have been suggested. The phase accuracy of the timing system has been specified to fulfill the desired image resolution. A novel way to calibrate the imaging system has been proposed using the phases obtained from measurements of the usual incoherent scattering signals. The inversion algorithm based on the Maximum Entropy Method (MEM) has been implemented and tested on simulated and real data, the latter obtained with the imaging-capable radar of Jicamarca. Methods to represent visually a function of five independent variables—with various degrees of completeness and compression—have been investigated and tested with simulated data and real world data (from Jicamarca). A brief summary of the physico-mathematical foundation of Aperture Synthesis Imaging Radar, ASIR, is included.

2. Introduction

This chapter on Work Package 5: Interferometry, contains two sections (3 and 4) on the technique used for imaging with a radar. Section 3 is a qualitative and succinct description of how the technique works, while section 4 contains the physical and mathematical foundations described in a brief manner. The remaining sections (5-11) contain brief summaries of the reports and deliverables that were produced during the lifetime of the project. The section titles are live links to the original reports in the [EISCAT_3D web site](#). Sections 12, 13 and 14 contain a list of web links to all the reports and deliverables of WP5, an Appendix and the list of references respectively. The Appendix describes briefly the initial idea on interferometry with one baseline that was to become the Aperture Synthesis Imaging Radar (ASIR) technique. Finally section 15 contains acknowledgments and an alphabetic list of the individuals who have made contributions to Work Package 5.

3. Radar Imaging in a nutshell

The technology employed is Aperture Synthesis Imaging Radar (ASIR) and is closer to the technology used by radio astronomers (VLBI, Very Long Baseline Interferometry) to image stellar objects (Taylor et al., 1999) than to the SAR (Synthetic Aperture Radar) technique used onboard airplanes and satellites to map the Earth's surface and other planetary surfaces. In the radio astronomy case the source itself spontaneously emits radiation that is collected by a number of passive antennas. In the former, the radar transmitter—acting

exactly like a camera flash—illuminates the target (the ionosphere or atmosphere) and a number of antennas collect the scattered radiation—exactly as in the radio astronomy case (or like the lens of a camera). From this point on, the two cases are essentially identical (Earth’s motion is an important difference). The procedure to construct the image of the target consists in calculating the cross-correlation between the signals from all different pairs of receivers. These values represent samples of a function in two dimensions called the visibility. The two space dimensions are the positions of the pair of receivers, known as baselines; specialized to the usual case in which the baselines are contained in a plane. The imaging inversion problem consists in obtaining the image from the visibility, which, in principle, should be a 2-Dimensional Fourier transform. However, in virtually all cases, the samples of the visibility are sparse, uneven and truncated, which leads to a highly singular inversion problem requiring carefully crafted algorithms. The image obtained from the inversion algorithm is called the brightness distribution, or just brightness, and (for each range), it is a function of the angle of arrival of each point in the target, that is, the brightness is the angular distribution of the target’s intensity. In the radar application it is often advantageous to first decompose the receiver signals into their spectral (frequency) components and apply the imaging inversion to each spectral component separately to obtain one image per spectral component. It is a non-trivial task to express visually the image as a function of three space variables, one frequency variable, and time, in all, five independent variables. The time variable can be taken care of by displaying images (frames) in rapid succession, that is, in the form of an animation or movie. There still remains four independent variables of which only two can be employed using conventional plotting techniques. Since the mathematical relationship between the visibility and the image is a simple (2-D) Fourier transform, all the accumulated applied knowledge on Fourier transforms in other domains can be applied to imaging. For instance, the resolution of the image is determined by the longest distance between receivers (longest baseline); the larger structures (bandwidth) are determined by the shortest baseline; resolution and bandwidth are related by the Nyquist theorem; windowing effects and their mitigation are the same; and so on.

In Work Package 5 of the EISCAT 3D project we have established all the conditions and parameters relating to the description just given above—for the new radar to have a 3-Dimensional capability. The core antenna will be composed of 20 or more modules (sets of 343 or 49 antenna elements) accompanied by a few outlying modules, the latter to comply with the resolution requirements. This is an optimum and flexible antenna layout from which favourable configurations can be quickly implemented to obtain the angular resolution and coverage of the required image; several simulated configurations have been suggested. The phase accuracy of the timing system has been specified to fulfill the desired image resolution. A novel way to calibrate the imaging system has been proposed using the phases obtained from measurements of the usual incoherent scattering signals—for which these radars are designed. The inversion algorithm based on the Maximum Entropy Method (MEM) has been implemented and tested on simulated and real world data, the latter obtained with the imaging-capable radar of Jicamarca. Methods to represent visually a function of five independent variables—with various degrees of completeness and compression—have been investigated and tested with simulated data.

It is the imaging capability of the future EISCAT 3D radar that will justify the 3D in its name. However, it is the quantum leap in quantity and quality provided by the imaging capability that will make the future EISCAT 3D radar unique in its category to produce world class atmospheric and ionospheric science at arctic latitudes.

4. The aperture synthesis imaging radar interferometer

The reasonable assumption is made that the target after it has been illuminated by the radar behaves as a thin (in range) source whose structure we wish to find, that is, we wish to measure the image of the target/source. Under a few additional basic assumptions (Clark, 2001), most notably, that the source is spatially incoherent and quasi-monochromatic and that Huygens' Principle is valid, the cross-correlation between the points \mathbf{r}_1 and \mathbf{r}_2 of the far field of the source is, to a very good approximation:

$$V_\omega(\mathbf{r}_1, \mathbf{r}_2) = \int B_\omega(\mathbf{s}) \exp[-i\omega \mathbf{s} \cdot (\mathbf{r}_1 - \mathbf{r}_2)/c] d\Omega \quad (1)$$

where $B_\omega(\mathbf{s})$ is the angular brightness distribution in the direction of the unit vector $\mathbf{s} = (l, m, n)$; l, m, n , are the direction cosines (components) of the vector \mathbf{s} ; the integration is over a unit sphere. We specialize this general result to the case of aperture synthesis with the additional assumption that the measurements of the cross-correlation are confined to a plane, as is the case of the radar application. The vector spacing (baselines) between all pairs of measurement points is conveniently expressed in wavelengths, $\lambda = 2\pi c/\omega$, $\mathbf{r}_1 - \mathbf{r}_2 = \lambda(u, v, w)$, which becomes $\mathbf{r}_1 - \mathbf{r}_2 = \lambda \cdot (u, v, 0)$ after choosing the measurement plane $w = 0$. In this coordinate system, the components of the unit vector \mathbf{s} are $(l, m, \sqrt{1 - l^2 - m^2})$ and the solid angle element $d\Omega = dl dm / \sqrt{1 - l^2 - m^2}$ resulting in

$$V_\omega(u, v) = \iint \frac{B_\omega(l, m)}{\sqrt{1 - l^2 - m^2}} e^{-2\pi i(ul+vm)} dl dm. \quad (2)$$

This integral has the form of a 2-D Fourier transform: In nearly all cases the target occupies a very narrow angular region implying that the brightness is non-zero only within a small interval of (l, m) values near the origin, that is $l, m \ll 1$. Thus the integration range can be extended to comprise the whole lm -plane. Then the brightness can be inverse-transformed from the visibility:

$$\frac{B_\omega(l, m)}{\sqrt{1 - l^2 - m^2}} = \iint V_\omega(u, v) e^{2\pi i(ul+vm)} du dv. \quad (3)$$

In an actual experiment the measurement of the visibility is discrete, sparse and uneven. The previous equation is modified as follows:

$$B_\omega^D(l, m) = \iint V_\omega(u, v) S(u, v) e^{2\pi i(ul+vm)} du dv \quad (4)$$

where $S(u, v)$ is the sampling function and $B_\omega^D(l, m)$ is called the *dirty* image. At this stage, the square root factor can either be ignored (since $l, m \ll 1$) or taken into account in $B_\omega^D(l, m)$. In actual practice, the dirty image is greatly distorted and is only used as an initial input to more effective restoration or inversion algorithms as described later. We make clear that the restoration of the image involves two operations, namely deconvolution and Fourier transformation. Using the convolution theorem:

$$B_\omega^D(l, m) = B_\omega \star G \quad (5)$$

where the star operator denotes convolution and the point spread function (also called synthesized beam, or impulse response, or Green function) $G(l, m)$ is the Fourier transform of the sampling function:

$$G(l, m) = \iint S(u, v) e^{2\pi i(ul+vm)} du dv. \quad (6)$$

There are two other effects that distort the measured brightness that are usually small and will be ignored in this treatment for the sake of clarity. These are the finite width of the antenna beam elements and the finite bandwidth of the receivers. The correction for the former is unproblematic while the effects of the latter can be made negligible by using a sufficiently narrow bandwidth.

Here is the *crux* of the matter: How to deconvolve Eq. (5) to obtain the *clean* brightness. In nearly all cases of interest the deconvolution as such cannot reproduce the true visibility because the problem is highly singular: $V_\omega = V_\omega^D/S$, where V_ω^D is the measured visibility. The sampling function S is a very spiky function (δ -functions) full of holes over large regions of the uv -plane where no measurements were made. Thus, the division by S is undefined over these regions because S is zero in those regions. This implies, in strict terms, that the actual visibility is unrecoverable, and so is the brightness.

However, from the mathematical viewpoint of inversion theory there exists a large class of solutions, namely a large class of brightness distributions, that all have exactly the same measured visibility V^D . One brightness solution distinguishes from the others in that its corresponding visibility reproduces the values of the visibility that were measured and evaluates to zero at points where no measurements were done. These null points are the points of the true visibility function that were multiplied by the zeros of the sampling function [the integrand of Eq. (4)]. Thus the most general solution is the sum of the principal solution plus brightness functions obtained from visibility functions defined in arbitrary ways in the regions where the sampling function is zero, and zero outside those regions. The latter have been called “invisible distributions” by Bracewell (2004). There is another way to describe the results of this analysis. Mathematically the problem is to solve an inhomogeneous integral equation. The most general solution of inhomogeneous equations can be expressed as the sum of the particular solution—what we have called the principal solution—plus the solutions to the homogeneous equation—what we have called the invisible distributions. The latter is the null space of the operator that defines the equation to be solved. Ultimately the measure of success of image restoration boils down to adopting a proper choice strategy to pick out one member of the invisible distributions. This amounts invariably to extrapolation.

The unavoidable presence of noise forces a degree of ambiguity in any case, even if the visibility is sampled to perfection. The task is now to construct numerical algorithms that narrow the choice in a systematic manner employing sensible choice criteria (constraints) and using a priori information whenever available. The expectation is that among a certain class of solutions there will be one or a few solutions that represent the true image in a satisfactory manner. Fortunately, this turns out to be the case. One such methodology is the CLEAN algorithm (Cornwell, 2001) which is a heuristic iterative procedure based on the assumption that the image is composed of a set of point sources (targets). Another approach that has a more developed mathematical foundation is the Maximum Entropy Method (MEM). It is founded on the concept of entropy derived from statistical mechanics and information theory. The idea is to single out a region of the solution space that is compliant with basic properties of an image function, notably positiveness, and choose the one solution that makes the least assumptions about the image. Expressed in mathematical terms, the problem is to find a function that maximizes the entropy functional, called \mathcal{H} , over the space of allowed solutions. Here is another *crux* of the matter: The form of the entropy functional is not unique (in contrast to statistical mechanics) and there are no clear criteria for how to define it. One discrete form, among the many that can be found in the

literature (Cornwell, 2001), is the following:

$$\mathcal{H} = - \sum_k B_k \ln \frac{B_k}{eM_k} \quad (7)$$

where B_k are samples of the brightness, \ln is the natural logarithm, $e = 2.71 \dots$ its base, and M_k is a default image that allows the introduction of a priori information. These two algorithms have been used successfully by radio-astronomers to obtain images of stellar objects. Scientists of the Jicamarca Radio Observatory have used the MEM to obtain images of ionospheric plasma turbulence with considerable success (Hysell and Chau, 2006).

Since, in principle, the relationship between the brightness and the visibility is a Fourier transform, there are several general consequences that are very useful to investigate beforehand in order to define a viable and good experimental design. The sampling theorem states that the sampled function must be band limited in order to avoid aliasing. Indeed, the measurement procedure in a natural manner ensures the compliance with this condition since the finite width of the antenna beams plays the role of an anti-aliasing filter. Furthermore, the tapered nature of the beam pattern plays the useful role of windowing that reduces sidelobes introduced by the filter (at the expense of losing some angular resolution).

5. Considerations and requirements regarding Interferometry (September 2005)

This report deals with recommendations regarding general and elementary conditions that have to be fulfilled by a phased array radar in order to have built-in imaging capabilities touching upon the lengths and number of the baselines, the placement of the antenna elements, the active elements, the receiving elements, and signal processing.

The properties of the Fourier transform imply that the shortest baseline determines the angular size of the image (bandwidth in Fourier parlance). Thus, the distance between neighbouring antenna modules is what will determine the maximum angular extent of the image. Assuming that the length of a module is 16λ (WP3 Report) the angular coverage will be $1/16$ radians or about 3.6° which translates into a horizontal size of about 6 km at 100 km range and 18 km at 300 km range. However the image size will be determined by the size of the illuminated volume which is considerably smaller. In the case of strong signals it will be advantageous to utilize a compact subset of the entire array for transmission to cover a wider illuminated beam, consequently a wider image. Since the transmitted power is distributed, there will be a proportional loss of power. A more effective and elegant alternative is to use aperture illumination coding that employs the entire array (Woodman and Chau, 2001).

The longest baseline will determine the angular resolution of the image. It is expected that the smallest scattering structures will be encountered in the auroral E-region, as optical measurements indicate the existence of structures of some tens of metres in visible aurora (Trondsen and Cogger, 2001). A useful target resolution is therefore a structure of 20 metres width at 100 km range that subtends an angle of 2×10^{-4} radians which implies a baseline length of 5000λ or 6250 m for a radar frequency of 240 MHz. Since the dimension of the core array will be at most in the few 100 metre, a few outlier antennas have to be built.

The number of samples of the visibility function that can be measured is equal to the number of different baselines which in turn is equal to the number of different receiving antenna pairs, or $n(n - 2)/2$, where n is the number of receiving antennas. Allowing for 4-10 outlier antennas, the remaining will be taken from modules in the core array.

The number of the latter will depend on the total number of modules and on their size. Images of reasonable quality have been obtained by a relatively small number of antennas at the Jicamarca Radar, of the order of 6-8 under high signal to noise ratio conditions. At least as many will be supported by the E-3D radar. For instance the combination of 8 core modules and 4 outliers will give 66 baselines (somewhat less if there are redundant baselines). Various optimum baseline configurations and signal processing for real-time monitoring are the subject matter of the Configurations Report of September of 2006 that is summarized below.

6. Fundamentals of radar interferometry I: One baseline Stage 2 report (April 2006)

This report contains the full derivation of basic expressions for the observable complex cross-correlation and complex coherence in a two-element radar interferometer. The expressions are two-dimensional generalizations of the one-baseline interferometer with arbitrary orientation employing separate antennas for transmitting and receiving. The Appendix contains a simplified derivation, the results of which have been employed in the processing and interpretation of interferometric measurements using the EISCAT Svalbard Radar (Grydeland et al. 2003) and in the early experiments made at the Jicamarca Radar (Farley et al., 1981). The report includes the definition of the terminology employed in the field and a preliminary discussion of signal processing requirements to monitor the ionospheric targets in real time searching for high coherence events.

7. Report on Synchronisation for interferometry (September 2006).

In this report it is shown that the phase of the measured visibility function depends linearly on the time delay between the signals arriving at the two antennas of a baseline. Furthermore, one phase period maps to one fringe period, and each of these to one radio-wave period. Thus, a useful condition on the accuracy of the phase—which determines the quality of the measured image—is that the random variations (time jitter) of the timing system, δ , should be a small fraction of the period of the radiation (the radar), $\delta \ll T_o$, T_o being the period of the radiation. A practical condition can be that the total phase inaccuracy be about 10° , or 1/40th of a period, which gives 100 ps for a 250 MHz radar. In fact, the random time variation in this condition should be the accumulated random time variation. Since the accumulated random time variation decreases in proportion $1/\sqrt{n}$, where n is the number of accumulations (when the jitter is statistically independent) the actual allowed time jitter is decreased by this factor. For instance, beam forming is performed by the addition of simultaneous samples (multiplied by phase factors) taken from a number of antenna elements, usually the elements of a module. For 343 elements to a module, the allowed time jitter of the individual samples will be reduced by a factor of $\sqrt{343} \approx 20$, or 2 ns instead of 100 ps.

8. EISCAT-3D Radar Imaging Arrays Configurations Report (September 2006)

The meeting between WPs 4, 5, 8 and 9 held in Kiruna in early July of 2006 led to the adoption of a two-level beam forming architecture (McKay, 2006). This architecture, when compared to others that were under consideration, is simpler to implement and produces the desired results for the full array beams, while it eliminates the need for separate beam formers for interferometry, increases the configuration flexibility considerably, and it immediately provides interferometric capability for all receiver beams. It is an optimum global solution that satisfies the requirements of interferometric imaging, as the module antennas of the second level constitute the antenna units upon which antenna baselines can be

constructed with great flexibility under software control, very possibly at the experiment design/implementation level. The configurations that can be obtained are limited only by the size of the modules in the first level and by the longest linear dimension of the entire array. An important task of the design process is then to survey the parameters of the limiting configurations on the basis of this architecture. Advantageous geometric patterns into which the module antennas can be organized into baselines are described for various sizes and geometries of the core array.

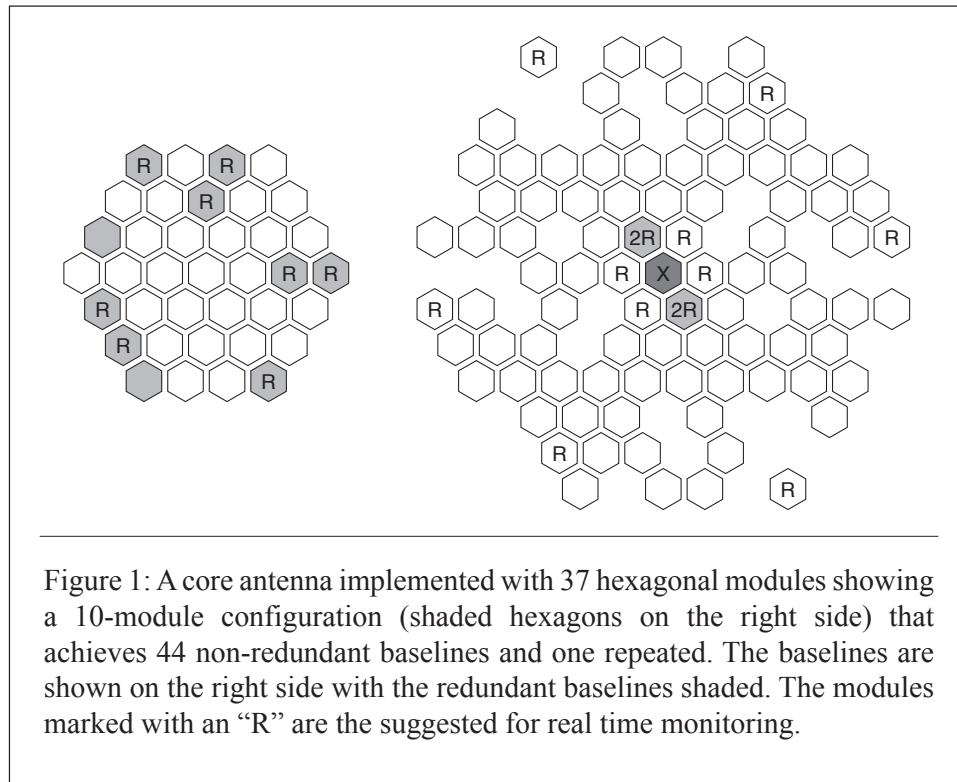
The two-level beam forming architecture consists in combining the signals into beams in two stages. In the first stage, module beam formers (BF) will apply a Delay-Phase shift and Add (DP/A) operation to antenna element amplitudes and accumulate the results for groups of 343 elements to form module beams (module beams of 49 elements will also be possible). On entering the second level there is a bifurcation: the module beams from all modules are added to form the full beam; then the same module beam signals are routed to the interferometric sub-system (IRX) where they are downsampled to a bandwidth matched to ion line observations. The module beam signals are the starting points for interferometric signal processing and storage.

The purpose of the real-time processing is to decide when to store amplitude data from the interferometry sub-system. The production of images from the amplitude data that is stored will be made offline. It is sufficient to monitor a small number of baselines distributed in orthogonal directions in real-time in order to detect interesting events and trigger the storage of the data streams by thresholding. Profiles of cross- and auto-correlation and complex coherence functions of a selected set of modules will be calculated in real-time. Any one or all of these functions will be thresholded in order to decide whether to store the data streams or not. The selection criteria may use low threshold values to begin with, to allow for some false positives (data stored without interesting features) and minimise the number of false negatives (interesting events lost). With experience, threshold adaption will be utilized. Temporary storage of amplitude data in ring buffers will allow the permanent storage of data 1/2 to 1 second prior to a triggered event and to continue for as long after the end of an event. The records will incorporate the selection criteria that originated the trigger and the corresponding range. Generally, the smallest scattering structures will produce higher coherence regardless of baseline, while larger structures will only produce high coherence from shorter baselines. Thus, an initial strategy on the choice of which baselines to monitor in order to catch as many events as possible would be to monitor a couple of short and a couple of intermediate baselines oriented N-S and E-W respectively.

Data for interferometry will be stored as amplitude data. This is a consequence of the fact that with an integration time of 0.1 s, the storage requirements are still smaller for amplitude data than for the quadratic quantities such as correlated or spectral data—the reason being that the number of baselines increases quadratically with the number of modules used for interferometry. In addition storing the amplitude data gives added flexibility during the offline processing of the data.

The design of module configurations suitable for imaging has been divided in two parts: configurations for the core (involving a subset of the core modules), and configurations of outlier modules. Randomly placed modules, as well as optimally selected subsets of various regular (dense) arrangements have been analysed for the core configurations. An optimal configuration is one that fills maximally the baseline space (the u - v space of the visibility function). That means generally the most even distribution of baselines with a minimum of redundant baselines. The specifications are given by the number of baselines and their

placement on a two-dimensional coordinate system. This is done best graphically as in Figure 1 which includes the antenna module configuration itself and the distribution of baselines (the sampled points of the visibility) side by side. A few configurations have been also illustrated with their synthesized beams. A nice example is described in this summary. This is a core array using 37 hexagonal modules in a hexagonal grid of 7 lines shown on the left side of the figure. A configuration of 10 modules—shown shaded on the left side of the figure—has been found which achieves 44 non-redundant baselines with only one repeated baseline indicated by the two shaded hexagons on the right side of the figure which shows the baseline coverage. The modules and baselines to be used for real-time monitoring are marked with an “R”.



For sizes of the core array under consideration of the order of one hundred metres (80λ) it will be necessary to deploy outlier modules, which are assumed to be identical as the core antenna modules. The core modules will provide the short baselines and their particular imaging configuration will not have a decisive impact on the configuration of the outlier modules. Thus, a 21-module core with an 8-module configuration for imaging was employed for the simulations carried out for this report. The guiding principle is that the synthesized beam shall have a minimum of artifacts, e.g. sidelobes. Therefore, the synthesized beam should be as clean as possible in order to give the image inversion algorithm a good initial estimate. Module configurations were evaluated by the maximum sidelobe level in the synthesised beam inside a region in the vicinity of the on-axis position. Based on experiences from radio astronomy, nominal module positions were sought along log-spiral arms. To take advantage of the property of random distributions to have a tendency to produce low sidelobes, the starting point was a random distribution of 100 module antennas spread along a log-spiral path of appropriate size. A sample of 9 modules with favourable sidelobe properties were taken from this distribution based on 9 nominal positions. We refer to the

reader to the original report for the detailed results.

It is clear that the particular configurations described are among many others also with favourable properties that could be considered. The main point is that at this stage of the design activity it is more important to establish the criteria and methods of selection rather than to specify a definitive configurations which should be done at a later stage of the design and implementation of the project.

9. Radar Interferometer Phase Calibration using the Visibility function of Incoherent Scattering (May 2007)

During some of the early interferometric experiments carried out using the two antennas of the EISCAT Svalbard radar, Grydeland (2007) discovered that the phases of the complex coherence function of incoherent scatter signals were very well ordered—that is, they were approximately constant within the signal bandwidth of incoherent scattering—even when the amplitude of the coherence was rather low. It was promptly realized that what was going on is as follows.

Under normal and quiet situations, the ionosphere is homogeneous within scale lengths much larger than a typical horizontal extent of the transmitter antenna beam over much of the ionosphere, certainly up to and well above the peak of the F-layer. In this situation, and under the most general conditions regarding the geometry of a radar interferometer, it turns out that the visibility function (the complex cross-correlation between two separated receivers) has a constant phase equal to zero, that is, the visibility is a real number. This affords a convenient method for global relative calibration of the baseline phases of an aperture synthesis radar used for ionospheric imaging, as Grydeland had suspected.

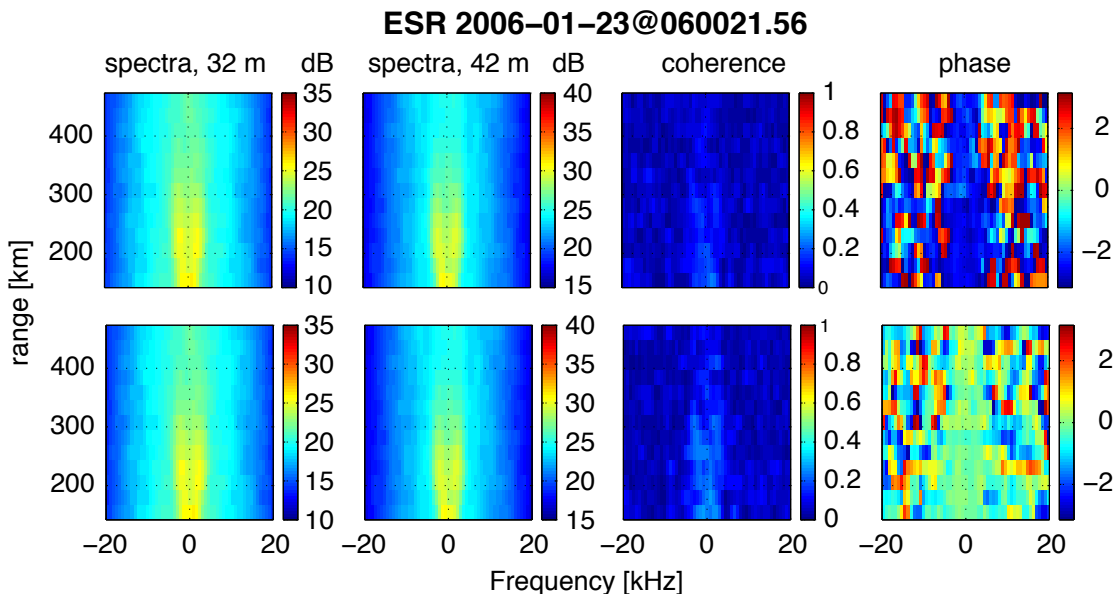


Figure 2. Spectra and complex coherence measured by the ESR. The phase in the lower panel has been calibrated by subtracting the measured phase shown in the first panel. A slight improvement of the coherence amplitude can be appreciated.

Figure 2 shows an illustrative measurement and its calibration. The upper panel shows

from left to right two frames with spectrograms of IS signals measured by the 32 and 45 metre antennas of the EISCAT Svalbard Radar, respectively, while the third and fourth frames show the amplitude and phase of the coherence function of the two signals as a function of Doppler frequency. One can appreciate that the phases are constant within the bandwidth of the signals as defined by the power spectra shown in the first two frames. Likewise, the coherence amplitude of the signal is clearly delineated and stands out from the noise even when its value is very low. The second row shows the results after the calibration was performed. The procedure for this case of one baseline is simply to set the phases of each pair of signals equal to each other; or equivalently, of their coherence functions. One can verify that after the correction, the coherence amplitude has improved. One should not be misled by the ever slightly improvement seen in this example, which is not the object of the present exercise. In an actual imaging experiment, the visibility function is sampled at many points (baselines) and the quality of the resulting image after inversion/restoration depends decisively on the accuracy of the visibility phases. Generally, the calibrating phases are all the relative phase differences between all baselines, provided the brightness distribution is uniform, as is the case of incoherent scattering under normal conditions.

Many other calibration methods have been reported in the radio astronomy literature and recently also by investigators that employ the Jicamarca radar for ionospheric imaging (Chau et al., 2008). A relative simple but effective method of absolute calibration is to measure the radiation of a radio star of known position. The radio star appears to the radar receiver as a point source which results in clean and accurate phase and time delay measurements from which correction phases can be extracted.

10. Report on Image Inversion for Interferometry (August 2008)

Amongst the many image inversion/restoration algorithms employed by the much bigger radio astronomy community, two stand out, namely the CLEAN procedure and the Maximum Entropy Method (MEM) (Cornwell, 2001). After some considerations, it was decided to adopt the MEM algorithm for development and tests for this project. The CLEAN procedure assumes that the true image is composed of a small number of point sources—which is the case in many astrophysical situations, but not generally in the radar applications. The MEM has a more mature mathematical foundation and, in the version we have chosen, is effective and robust as shown by the Jicamarca implementation (Hysell and Chau, 2006). Briefly, the numerical problem is to find an extremum of the following functional, using Hysell’s notation and the Einstein summation convention:

$$E[f(e_j, \lambda_j, \Lambda, L)] = S + \lambda_j(g_j + e_j - f_i h_{ij}) + \Lambda(e_j^2 \sigma_j^{-2} - \Sigma) + L(I_i f_i - F) \quad (8)$$

where f is the sought after brightness distribution, $S = -f_i \ln(f_i/F)$ is the entropy [see Eq. (7)], I_i is a vector of ones, $F = I_i f_i$ is the integrated (total) brightness, g_j is the measured visibility, h_{ij} is the point spread function that contains the Fourier kernel, e_j are the random errors, σ_j^2 are the (theoretical) expected error variances, and Σ parametrizes the error norm, effectively constraining it. The remaining quantities are Lagrange multipliers as follows. λ_j defines the fundamental constraint on the entropy functional by relating the measured visibility (including the random errors) to the sought after brightness that makes the entropy functional an extremum. The other Lagrange multipliers put additional constraints that typically would ensure an improvement of the quality of the final solution: Λ puts a bound on the error norm equal to a preset value equal to Σ ; and L constrains the total brightness effectively ensuring that the solution will be non-negative (positive semi-definite).

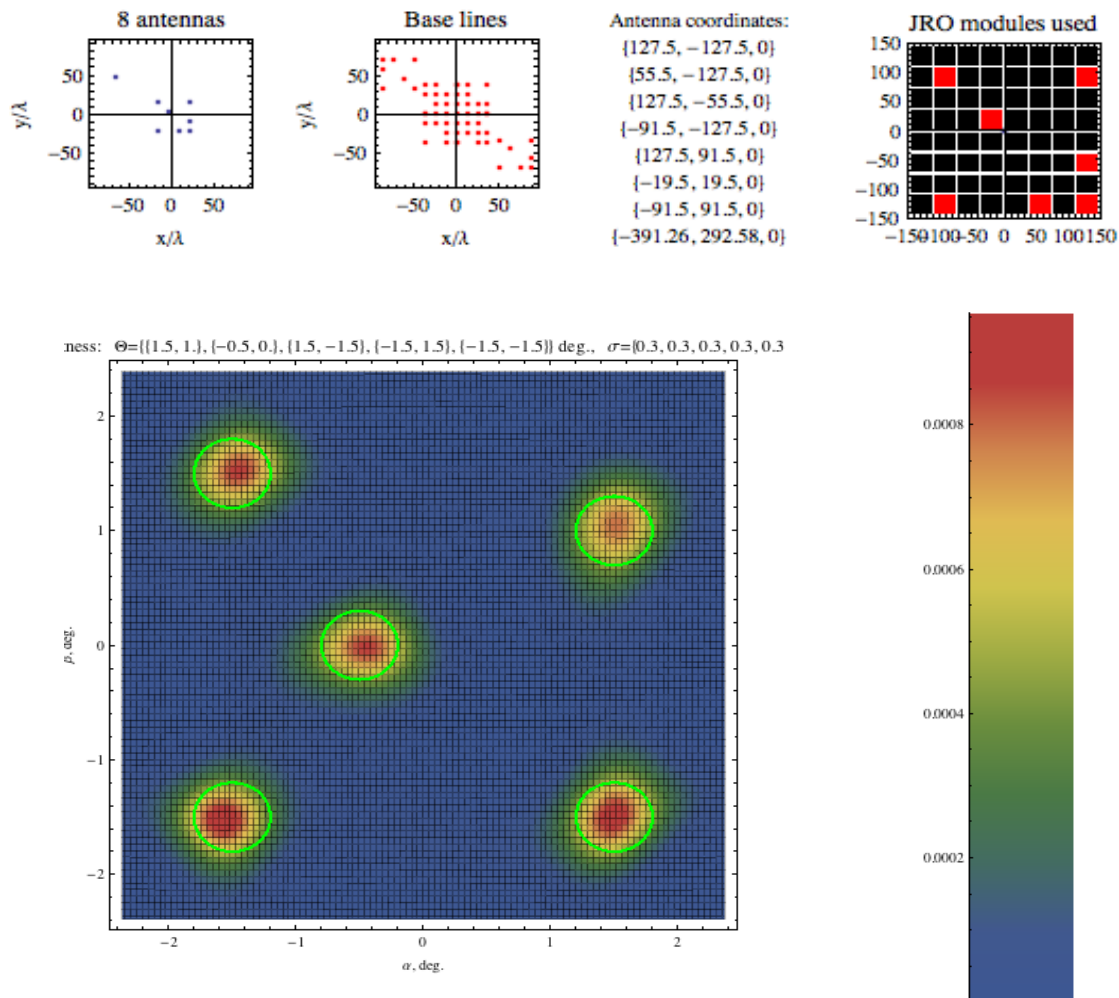


Figure 3. Five-blob image reconstructed from the visibility measured with the 8-antenna configuration with 7 core antennas of the Jicamarca array and 1 outlier shown in the upper left panel. The second upper left panel shows the baselines generated by the configuration. The right most upper panel shows the core antennas used in the configuration in red and their coordinates alongside. It is a remarkably optimum configuration that produces an excellent reconstruction.

The software implementing the algorithm has been written as a Mathematica package. The Mathematica application, with its powerful symbolic and numerical facilities, was considered advantageous to use in order to produce a first prototype in a short period of time. The algorithm has been tested on simulated data and on real world data taken with the Jicamarca Radar. An interesting configuration of 7 core modules and an outlier module was found that produces an evenly distribution of baselines coordinates with a minimum of gaps and was utilized in the tests. Figure 3 shows the configuration and the results of inverting an image composed of 5 localized gaussian blobs as described in the figure. The source code of the Mathematica package is available for download at the EISCAT_3D website.

11. Report on Multidimensional Imaging Radar Data Visualization (February 2009)

The problem of presenting the multi-dimensional brightness distribution data obtained from imaging radar in a way that its physical significance can be appreciated in a visually

intuitive manner is very challenging. Since the brightness distribution function is a function of five independent variables: three spatial coordinates (two bearing angles and range), Doppler frequency, and time, $B(\alpha, \beta, r, f, t)$, the problem is how to represent points of a 6-dimensional space on a two dimensional surface—usually on a computer monitor or on a sheet of paper. In fact, it is feasible to implement this representation by using the two spatial coordinates of the displaying surface augmented by the three values that define a colour, and animation to represent time. However, colour as representing three quantities (mathematically/physically correct), does not lend itself to an intuitive appreciation by the human brain (whether this skill can be gained by training is beside the point). A mechanism of dimension reduction is necessary.

A very powerful mechanism of dimension reduction (Thomas and Cook) is to use projections, the simplest and most versatile technique being just to collapse one or more dimensions by integrating the dimensions left out from the graphical representations. This technique is automatically multi-level and provides unambiguous data visualization at different levels of displayed details. At the first level all but one independent variable are integrated and the result can be plotted as a curve. For instance, one of these that has physical relevance is the total brightness as a function of time, the total brightness being synonymous with total power or intensity; in the case of pure incoherent scattering, the total brightness would be proportional to the total electron content (TEC). At the next level three independent variables are integrated leaving a function of two independent variables. A common case is when the surviving variables are range and time and the graphical representations are known as Range-Time-Intensity plots or RTIs which are usually represented as colour or gray scale maps or as contour plots. These two levels result in static plots. At the third level, keeping time and integrating any two of the remaining variables, one obtains plots as in the previous levels that can be animated by displaying them one at a time successively as a function of time, namely one produces a movie. For instance, dynamic spectrograms as a function of range and time. The fourth level exploits more fully the advantages brought about by imaging by integrating only one independent variable—which is not usually the time—and encoding the value of the brightness distribution and the Doppler frequency with two of the three variables of colour space. It is advantageous to use the Hue-Saturation-Value or HSV colour space with hue to encode the Doppler frequency and the saturation the brightness distribution keeping the third colour parameter—the value—constant, usually 100%, that is, only the brightest colour combinations are employed. The Doppler is conveniently divided in three regions of hue with green tones to encode frequencies around zero and blue and red tones to encode the blue and red shifted frequencies, naturally. As mentioned earlier, employing the three variables of the HSV colour space in order to make a dynamic (animated) graphical representation of the brightness distribution as a function of all its independent variables is not advisable since it appears difficult for a viewer of such representation to “decode” the colours into its three quantitative components in an intuitive manner. As things are, even the two-colour variable representation of the 4th level described above requires a little effort to “get used to”.

Cuts come to the rescue, in a way, since it avoids integrating one variable, and instead, replaces it with a cut. This is accomplished by setting up a 3-dimensional coordinate system of the three physical dimensions $[(x, y, z)$ or $(\alpha, \beta, r)]$ on the 2-dimensional displaying medium (the computer monitor) using perspective and displaying in it a cut through any of the three axes at a specified value. The cut is displayed as a colour map where brightness distribution is encoded by colour hue and Doppler by colour saturation of the map’s

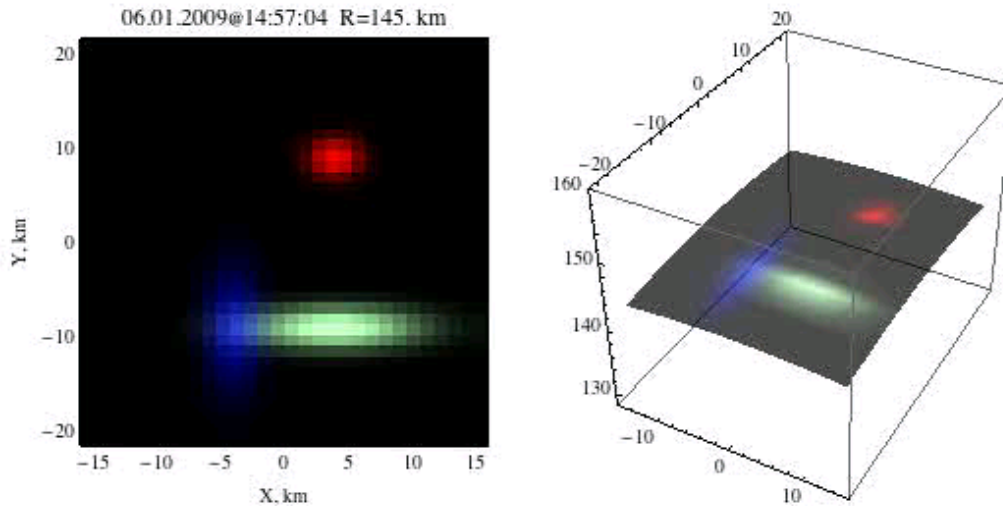


Figure 4. Cross section of simulated brightness data at a given range of $R = 145$ km.

pixels. Time is “encoded” by animation. Alternatively the cut can be displayed by itself as an animated colour map. Figure 4 shows an illustration in which both alternatives have been included and the cut has been made on the range axis at $R = 145$ km for simulated data. The figure is a live link, and clicking on it will transfer control to the user’s browser which will load and display the animation from the EISCAT_3D web site. The web site contains several illustrative examples of the visualization package for imaging developed for this project using simulated data and real data obtained with the Jicamarca radar, see below.

Prototype software to visualize the brightness distribution as described above has been developed as a Mathematica package *E3Dvisualize.m*. The package contains two basic functions for simulating (*SimulateBrightnessData*) and plotting the brightness data (*PlotImagingData*). To generate simulated multi-blob brightness data we use a Gaussian model of brightness distribution for each of a specified number of blobs with specified trajectories as a function of time. The programs and the examples can be downloaded from the EISCAT_3D web site.

12. List of live web links to reports and deliverables

1. Considerations and requirements regarding WP5: Interferometry, Sep 2005.
2. Fundamentals of radar interferometry I: One baseline Stage 2 report, Apr 2006.
3. Report on Synchronisation for interferometry, September 2006.
4. EISCAT_3D Radar Imaging Arrays Configurations Report, September 2006.
5. Radar Interferometer Phase Calibration using the Visibility function of Incoherent Scattering, May 2007.
6. Radar Imaging Algorithms Report, January 2008.
7. Final Radar Imaging Algorithms Report, August 2008.
8. EISCAT_3D Radar Multidimensional Imaging Radar Data Visualisation, March 2009.

13. Appendix: The one-baseline radar interferometer

The first application of interferometric methods in incoherent scattering radar was made

by Woodman (1971) who employed the large Jicamarca antenna array for transmission and two quarters of the antenna in a one-baseline configuration on reception to measure the local direction of the geomagnetic field with extreme accuracy. Farley et al. (1981) inspired by Woodman's work improved the method to include also frequency discrimination and employed it to make measurements of plasma turbulence in the equatorial electrojet above Jicamarca that revealed for the first time structure of the turbulence in the horizontal East-West direction. The principle of operation of the one-baseline radar interferometer relies on the measurement of the cross-spectrum between the two receivers which is the product of the amplitude spectra of both signals and can be represented as

$$V_1(\omega) = \sum_j A_j(\omega) e^{i\phi_j(\omega)} \quad \text{and} \quad V_2(\omega) = g \sum_j A_j(\omega) e^{i\phi_j(\omega) + i\Delta\phi_j}$$

where the phase of each harmonic component is the same for both receivers, ϕ_j , and has a uniform random distribution in $[0, 2\pi]$. The incremental phase of the second receiver, $\Delta\phi_j$, is due to the difference in path length of the radiation reaching both receivers:

$$\Delta\phi_j = kd \sin \theta_j \approx kd\theta_j$$

and g is a factor to account for gain differences between the two receivers. The complex normalized cross-spectrum is found to be

$$S_{12}(\omega) = \frac{\langle V_1(\omega) V_2^*(\omega) \rangle}{\langle |V_1(\omega)|^2 \rangle^{1/2} \langle |V_2(\omega)|^2 \rangle^{1/2}} = \langle e^{ikd\theta_j} \rangle = \exp\left(-\frac{1}{2} k^2 d^2 \sigma_\omega^2\right) e^{ikd\theta_\omega}$$

and is also known as the complex coherence function. In obtaining the last equality, it has been assumed that the θ_j have a Gaussian distribution with mean θ_ω and variance σ_ω^2 . The zenith angle θ_ω reveals the angular position of a discrete structure in the field of view of the radar and the variance σ_ω^2 the angular extent of the structure, both at the frequency ω , when the coherence amplitude is appreciable at the same frequency. Jicamarca scientists have applied the method with great success to study the structure of plasma turbulence that occur frequently in the equatorial ionosphere. Grydeland et al. (2003) employed the two antennas of the EISCAT Svalbard Radar, and using the same principles, found that enhanced radar echoes that occur during auroral precipitation (called NEIAL) are localized in filamentary structures with scale sizes of at most a few hundred metres in the plane perpendicular to the geomagnetic field.

14. References

- Bracewell, Ronald, *Fourier Analysis and Imaging*, 2004, Springer ISBN: 978-0-306-48187-1.
- Chau, J. L., D.L. Hysell, K.M. Kuyeng, and F.R. Galindo (2008), Phase calibration approaches for radar interferometry and imaging configurations: equatorial spread F results, *Ann. Geophys.*, 26, 2333-2343.
- Clark, B.G., *Coherence in Radio Astronomy*, Chapter 1 of Taylor et al., 1999.
- Cornwell, T., *Deconvolution*, Chapter 8 of Taylor et al., 1999.
- Farley, D. T., H. M. Ierkeic, and B. G. Fejer (1981), Radar Interferometry: A New Technique for Studying Plasma Turbulence in the Ionosphere, *J. Geophys. Res.*, 86(A3), 14671472.
- Grydeland, T., C. La Hoz, T. Hagfors, E.M. Blixt, S. Saito, A. Strømme, and A. Brekke (2003), Interferometric observations of filamentary structures associated with plasma

instability in the auroral ionosphere, *Geophys. Res. Lett.*, 30, 1338, doi:10.1029/2002-GL016362.

Grydeland, T., C. La Hoz and V. Belyey, Phase calibration of an aperture synthesis imaging array by means of incoherent scattering, Abstract (2007), 13th EISCAT International Workshop August 6-10 2007, Åland, Finland.

Hysell, D. L., and R. F. Woodman (1997), Imaging coherent backscatter radar observations of topside equatorial spread F, *Radio Sci.*, 32(6), 23092320.

Hysell, D. L., and J. L. Chau (2006), Optimal aperture synthesis radar imaging, *Radio Sci.*, 41, RS2003, doi:10.1029/2005RS003383.

Kudeki, E., and F. Sürücü (1991), Radar Interferometric Imaging of Field-aligned Plasma Irregularities in the Equatorial Electrojet, *Geophys. Res. Lett.*, 18(1), 4144.

McKay, D.J., EISCAT-3D WP4/5/8/9 signal processing meeting. summary of discussions from the meeting at 2006-07-03, 05.

Taylor, G.B. (Ed.), C. L. Carilli (Ed.) and R. A. Perley (Ed.) (1999), *Synthesis Imaging in Radio Astronomy II*, ASP Conference Series, Vol. 180; xxxiii, 704p; California, USA; ISBN 1583810056.

Thomas, J.J., and K.A. Cook, Illuminating the Path: The Research and Development Agenda for Visual Analytics. National Visualization and Analytics Center (NVAC). Online http://nvac.pnl.gov/docs/RD_Agenda_VisualAnalytics.pdf

Trondsen, T. S., and L. L. Cogger (2001), Fine-scale optical observations of aurora, *Phys. Chem. Earth (C)*, 26 (1-3), 179188, doi:10.1016/S1464-1917(00)00105-7.

Woodman, R. F. (1971), Inclination of the Geomagnetic Field Measured by an Incoherent Scatter Technique, *J. Geophys. Res.*, 76(1), 178184.

Woodman, R. F. (1997), Coherent radar imaging: Signal processing and statistical properties, *Radio Sci.*, 32(6), 23732391.

Woodman, R. F., and J. L. Chau (2001), Antenna compression using binary phase coding, *Radio Sci.*, 36 (1), 4551, doi:10.1029/2000RS002388.

15. Acknowledgments and Contributors to WP5

We thank Dr Jorge Chau, Director of the Jicamarca Radar Observatory, for his generosity in providing access to the Jicamarca Radar to conduct imaging experiments and tests and for very useful support and insights on the radar imaging technique. We also thank Dr Dave Hysell for no less very useful support and insights on the technique and for generously hosting one of us.

Vasyl Belyey	University of Tromsø
Tom Grydeland	University of Tromsø (now at Discover Petroleum)
Cesar La Hoz	University of Tromsø